PAPER

Check for updates

Colorimetric point-of-care diagnostic to monitor *Enterococcus faecalis* causing urinary tract infection

Maria M. Morim, [ID] [a] Patrick Rupper, [ID] [b] Stefanie Altenried, [ID] [c] Adrian Meier, [a] René M. Rossi, [ID] [a] Qun Ren, [ID] [c] Luciano F. Boesel [ID] [a] and Giorgia Giovannini [ID] *[a]

Urinary tract infections (UTIs) are among the most common bacterial infections, affecting approximately 150 million people worldwide each year. Currently, diagnosis is often made using culture-based methods, which are time-consuming and therefore costly. Point-of-care (POC) devices have the potential to provide a rapid and accurate UTI diagnosis, thereby improving treatment efficacy. In this work, we developed a fast, specific, and accurate colorimetric sensor capable of indirectly detecting *Enterococcus faecalis* in urine samples by targeting its metabolite, L-lactate. The sensing probe consists of silica nanoparticles (SNP) loaded with MnO_2 (MnSNP), functionalised on the surface with the enzyme lactate oxidase (Lac@MnSNP). The sensor enables both qualitative analysis – through a visible colour change – and quantitative analysis, using spectroscopy. The morphology and composition of the probe were characterised at each synthesis step, confirming that the incorporation of MnO_2 into SNP and subsequent enzyme functionalisation did not alter nanoparticle morphology. Lac@MnSNP demonstrated responsiveness to L-lactate, showing a linear decrease in signal up to 50 µM of the analyte, with a limit of detection of 31 µM. The probe successfully detected *E. faecalis* in artificial urine medium and in complex samples at concentrations as low as 10^3 CFU mL^{-1} within 5 h. These results demonstrate the potential of this probe for fast, accurate, and lactate-specific diagnoses.

Introduction

Urinary tract infections (UTIs) are among the most prevalent bacterial infections, affecting approximately 150 million people globally each year, with a particularly high incidence in women.[1] UTIs are also common in catheterised patients, where they can potentially prolong hospitalisation and contribute to an estimated annual societal cost of $3.5 billion in the United States alone. UTIs are associated with considerable morbidity, particularly in individuals with underlying comorbidities or those who are immunocompromised.[2]

Clinical diagnosis of UTIs relies on urine culture, which enables the identification of the causative bacterial pathogen. However, as culture-based methods are often time-consuming, antimicrobial treatments are often prescribed without clear

evidence of infection, contributing to the rise in antimicrobial resistance (AMR).[3]

Point-of-care (POC) devices offer substantial advantages over conventional diagnostic methods by enabling rapid and accurate diagnosis, which in turn supports timely and appropriate treatment. According to the World Health Organization (WHO), effective POC diagnostics should meet the ASSURED criteria: affordable, sensitive, specific, user-friendly, rapid and robust, equipment-free, and derivable to end-users.[4] A widely used POC device commercially available for UTI diagnosis is the dipstick assay. Dipsticks enable rapid, routine qualitative analysis of urine samples, typically through colorimetric changes that indicate parameters such as pH.[5] For more advanced, multisensing quantitative analysis, larger strip-based instruments – such as the Urisys 1100® Urine Analyzer or the LAURA® Semi-Automated Urine Strip Reader – are utilised. Despite the accessibility and ease of use, urine test strips have notable limitations in terms of detection range and sensitivity. They typically assess physical and chemical properties of urine (*e.g.* pH), which are not directly indicative of bacterial infection. As a result, they are more suitable for preliminary screening rather than definitive diagnosis.[6] Furthermore, urinary composition can be influenced by

[a] Empa, Swiss Federal Laboratories for Materials Science and Technology, Laboratory for Biomimetic Membranes and Textiles, Lerchenfeldstrasse 5, CH-9014, St. Gallen, Switzerland. E-mail: giorgia.giovannini@marionegri.it

[b] Empa, Swiss Federal Laboratories for Materials Science and Technology, Laboratory for Advanced Fibers, Lerchenfeldstrasse 5, CH-9014 St. Gallen, Switzerland

[c] Empa, Swiss Federal Laboratories for Materials Science and Technology, Laboratory for Biointerfaces, Lerchenfeldstrasse 5, St. Gallen 9014, Switzerland

11640 | *J. Mater. Chem. B*, 2025, **13**, 11640–11651

This journal is © The Royal Society of Chemistry 2025

metabolic, molecular, and genetic factors, potentially leading to misleading or inconclusive results[7].

Consequently, clinical practice continues to rely on laboratory-based techniques for bacterial identification and antimicrobial susceptibility testing. While these methods are accurate, they are time-consuming and delay the initiation of targeted treatment, thereby contributing to the spread of AMR.[8]

Given the substantial socioeconomic burden of UTIs and their contribution to the development of AMR, there is an urgent need to develop advanced POC diagnostic tools that enable rapid, accurate, and pathogen-specific detection to guide prompt and effective treatment. The POC device currently used, the dipstick, uses pH as a biomarker for the identification of UTI. However, pH is not necessarily correlated with infection. For a more accurate diagnosis, a POC device should be able to target bacterial-related biomarkers. Although UTIs can be caused by multiple bacterial species, _E. faecalis_ is an important cause in certain patient groups, such as those with catheter-associated or complicated UTIs.[2] _E. faecalis_ is a commensal, L-lactate-producing bacterium commonly found in the gastrointestinal tract, but it can become opportunistic when it colonises other organs, leading to infections such as UTIs. Its ability to form biofilms make these infections particularly difficult to treat, especially in catheterised patients, often resulting in a chronic infection.[8,9] Moreover, due to its ability to develop AMR and multidrug-resistance, _E. faecalis_ is listed in the "WHO Bacterial Priority Pathogens List (2024)" and is recognised as the third leading cause of nosocomial infections.[10–14]

L-Lactate is a versatile biomarker widely used in prognostic, diagnostic, and monitoring tools across a range of clinical conditions (_e.g._ infectious diseases, sepsis, trauma, and perinatal conditions)[15] and physiological states (_e.g._ monitoring athletic fatigue and workload).[16,17] L-Lactate-based sensors are most commonly designed for health monitoring applications, being also designed for food applications. Several POC devices for lactate testing are already commercially available, and they typically rely on colorimetric pH-based detection, since lactate accumulation leads to acidification of physiological fluids.[18,19] A more detailed review about lactate-based sensors can be found in ref. 15, 16, 20 and 21.

Colorimetric sensors offer several advantages for POC diagnostics, including a visible colour change that can be detected by the naked eye. These sensors are simple, specific, and sensitive, supporting the development of rapid, cost-effective, user-friendly, and affordable diagnostic tools that do not require complex or expensive equipment.[22–26] Direct detection of L-lactate has also been achieved using a limited number of recently commercialised electrochemical devices.[27,28] These systems, which directly target L-lactate _via_ enzymatic reactions, are widely used in clinical settings due to their rapid turnaround time and ease of use. However, a key limitation is the relatively high limit of detection (LOD), typically in the millimolar (mM) range, which restricts their applicability in diagnostic contexts that require detection in the micromolar (μM) range.[27,28]

In this work, we developed a rapid and cost-efficient colour-based detection mechanism for the indirect identification of _E. faecalis_ in urine samples, by targeting its metabolic by-product, L-lactate. The sensing probe (Lac@MnSNP) consists of silica nanoparticles loaded with manganese dioxide (MnSNP) and functionalised with the enzyme lactate oxidase. In the presence of L-lactate – produced by _E. faecalis_ – a cascade of enzymatic reactions is triggered, leading to the accumulation of hydrogen peroxide (H_2O_2). This accumulation reduces MnO_2 to MnO/Mn^{2+}, resulting in a visible colour change in the suspension from brownish to colourless. In addition to qualitative detection by the naked eye, the reduction of MnO_2 can be quantitatively monitored by measuring the decrease in absorbance at 400 nm. The probe was characterised at each stage of synthesis in terms of morphology, composition, and sensitivity to both L-lactate and _E. faecalis_. The sensor presented here offers a simple, user-friendly, and affordable POC diagnostic tool, with the potential to enable advanced, bacteria-specific detection for accurate diagnosis of UTIs caused by _E. faecalis_.

Results and discussion

The colorimetric sensor probe developed for the detection of lactate-producing bacteria, such as _E. faecalis_, is based on manganese dioxide nanoparticles (MnO_2) embedded within silica nanoparticles (MnSNP). The surface of these composite particles is subsequently functionalised with the enzyme lactate oxidase (Lac@MnSNP). The detection mechanism is illustrated in Fig. 1(A).

L-Lactate, released by the bacteria as a metabolic by-product of glucose fermentation, is oxidised by lactate oxidase on the surface of Lac@MnSNP. This enzymatic reaction produces H_2O_2, which subsequently reacts with the MnO_2 embedded within the silica core. The reduction of MnO_2 to MnO/Mn^{2+} results in the loss of the characteristic brown colour and the dissolution of the MnO_2 particles. The visible discolouration of the suspension serves as an indirect indicator of the presence of _E. faecalis_ in urine, suggesting a potential UTI.

The sensor is based on two essential components: (i) lactate oxidase, which serves as the sensing element by specifically recognising the target analyte L-lactate, a product of bacterial carbohydrate metabolism; and (ii) MnO_2 nanoparticles, which function as the transducer element, converting the biochemical detection of L-lactate into a measurable optical signal.

SNPs were selected as the structural scaffold between sensing and transducer elements due to their favourable surface chemistry and optical inertness, properties that facilitate this effective integration. Specifically, SNPs enable the stable immobilisation of lactate oxidase on their surface, promoting the localised production of H_2O_2 in proximity to the MnO_2 nanoparticles embedded within the silica core.

MnO_2 was synthesised by reducing potassium permanganate ($KMnO_4$) with ammonium hydroxide (NH_4OH), as shown in eqn (1) (Fig. 1(B)-i). The formation of MnO_2 molecules was monitored by measuring the absorbance spectrum of the
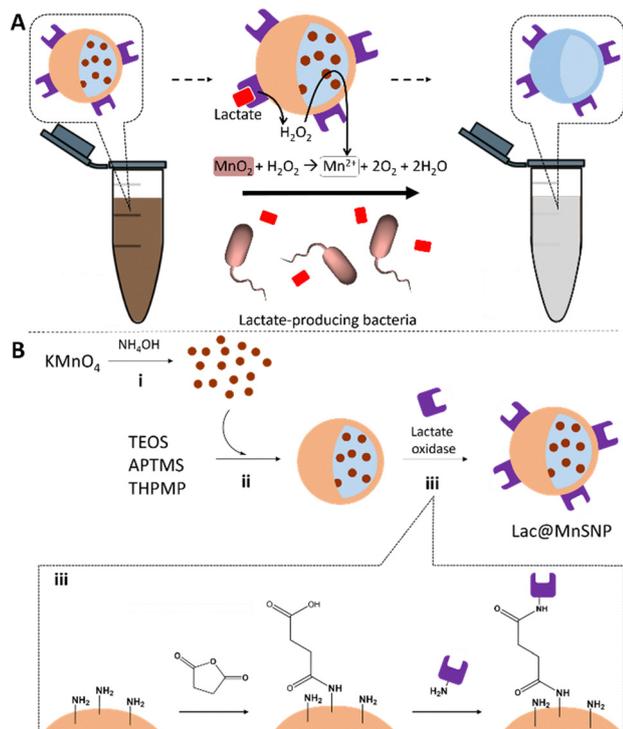
This journal is © The Royal Society of Chemistry 2025

J. Mater. Chem. B, 2025, **13**, 11640–11651 | **11641**

Fig. 1 (A) Schematic representation of the detection mechanism of the colorimetric probe for lactate-producing bacteria, such as *E. faecalis*. (B) Synthetic procedure for the preparation of Lac@MnSNP.

reaction over time. As shown in Fig. S1, the characteristic absorbance peaks of $KMnO_4$ at approximately 545 nm gradually disappeared, while a broad peak emerged around 350 nm, indicative of MnO_2 formation. These spectral changes confirmed the presence of MnO_2 after 40 minutes. The progression of the reaction was also visually evident from the colour change of the suspension – from purple ($KMnO_4$) to brown (MnO_2).

$$2KMnO_4 + 2NH_4OH \rightarrow 2MnO_2 + N_2 + 2KOH + 4H_2O \quad (1)$$
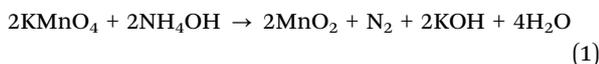
The aqueous suspension of the synthesised MnO_2 particles was employed as the water phase for the synthesis of core–shell silica nanoparticles using the microemulsion method (Fig. 1(B)-ii). Tetraethyl orthosilicate (TEOS) was used exclusively to form the silica core, while the shell was constructed using a combination of TEOS, a phosphate-containing silane – 3-(trihydroxysilyl)propyl methylphosphonate (THPMP) – and an amino-derived, (3-aminopropyl)trimethoxysilane (APTMS) silicate derivative. The amino groups present on the surface of the resulting MnSNP

were subsequently utilised to covalently conjugate the enzyme lactate oxidase through succinic anhydride linker (Fig. 1(B)-iii). The extent of enzyme immobilisation on the nanoparticle surface was determined by quantifying the residual protein content in the supernatant following particle purification by centrifugation. The calculated functionalisation was 83%.

The synthesised MnO_2, SNP, MnSNP, and Lac@MnSNP were morphologically characterised by dynamic light scattering (DLS) and transmission electron microscopy (TEM). The optimised synthesis of MnSNP produced a homogeneous suspension of nanoparticles with an average diameter of 158 ± 3 nm and a polydispersity index (PDI) of 0.17 ± 0.05 (Table 1). These results indicate that the incorporation of MnO_2 did not significantly alter the morphology of SNPs, aside from a slight reduction in size compared to SNPs (184 ± 2 nm size, PDI: 0.15 ± 0.02). DLS analysis of MnO_2 was inconclusive due to the small particle size and their tendency to form agglomerates, as confirmed by TEM imaging. TEM images of MnSNP demonstrated that the incorporation of MnO_2 did not alter the overall morphology of the silica particles (Fig. 2). In the case of Lac@MnSNPs, DLS revealed a significant increase in hydrodynamic diameter compared to MnSNPs, with a measured size of 1438 ± 52 nm and a PDI of 0.30 ± 0.02. However, TEM analysis showed that the core particle size remained small, with MnSNPs and Lac@MnSNPs exhibiting diameters of 153 ± 1 nm and 105 ± 1 nm, respectively. It was observed that the functionalisation of MnSNPs to form Lac@MnSNPs resulted in an increase in surface charge from −34 ± 1 mV (MnSNP) to −13 ± 1 mV (Lac@MnSNP). As the zeta potential approaches neutrality, the electrostatic repulsive forces between particles are reduced, promoting nanoparticle agglomeration in suspension, as indicated by DLS measurements. Nevertheless, TEM analysis confirmed that the nanoparticles retained their individual morphology despite the tendency to aggregate.

The elemental composition was examined using energy-dispersive X-ray (EDX) analysis. The detection of Mn in the MnSNP sample (Table 2) confirmed the incorporation of MnO_2 particles in the silica nanoparticle matrix. In addition, following treatment with H_2O_2, the MnO_2 particles were isolated *via* centrifugation, and EDX analysis revealed that the MnO_2 particles were completely degraded into soluble Mn^{2+} cations, as no pellet was observed after centrifugation of the MnO_2 sample. In contrast, EDX analysis of the pellet obtained after 2 hours of incubating MnSNP with 50 µM of H_2O_2 confirmed the degradation of MnO_2 while indicating the stability of the silica matrix. The MnSNP retained their morphology after treatment, with occasional signs of Ostwald ripening (Fig. 3), a phenomenon

Table 1 DLS and TEM characterisation of SNP, MnSNP and Lac@MnSNP

	DLS		TEM	
	Diameter (*Z*-average) [nm]	Polydispersity index (PDI)	Zeta potential (ζ) [mV]	Diameter (*Z*-average) [nm]
SNP	184 ± 2	0.15 ± 0.02	−25 ± 1	87 ± 1
MnSNP	158 ± 3	0.17 ± 0.05	−34 ± 1	153 ± 1
Lac@MnSNP	1438 ± 52	0.30 ± 0.02	−13 ± 1	105 ± 1

11642 | *J. Mater. Chem. B*, 2025, **13**, 11640–11651

This journal is © The Royal Society of Chemistry 2025
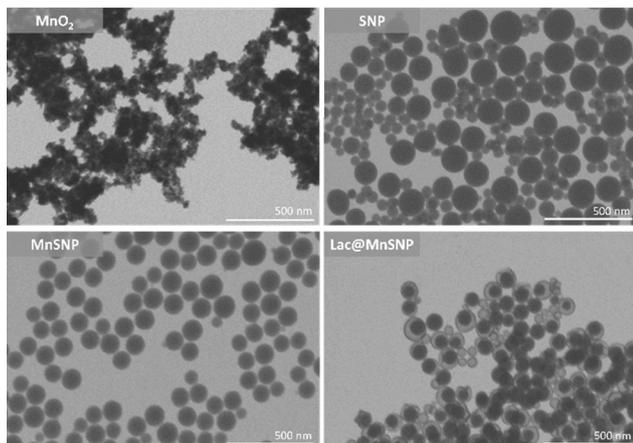
Fig. 2 Morphological characterization of MnO_2, SNP, MnSNP and Lac@MnSNP by TEM.
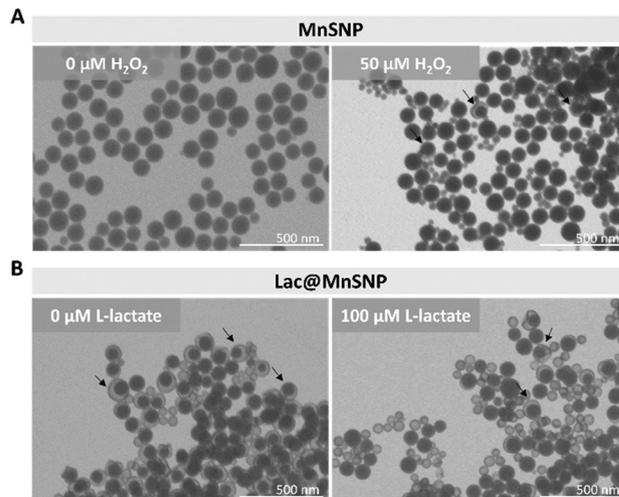

Fig. 3 Morphological characterisation of MnSNP and Lac@MnSNP by TEM, before and after interacting with H_2O_2 and L-lactate, respectively. (A) MnSNP and (B) Lac@MnSNP before and after interacting with H_2O_2 and L-lactate, respectively, where there were no significant differences between the different conditions. The black arrow present in the picture shows the occasional presence of Ostwald ripening.

that is typically observed in silica nanoparticles in aqueous environments,[29,30] where there is a structural rearrangement of the silica matrix forming the particles, and it is not indicative of degradation. Lac@MnSNP exhibited signs of Ostwald ripening from the time of synthesis (Fig. 3 and Fig. S2).

Notably, after 7 days of storage in deionised (DI) water, MnSNP exhibited a similar appearance as Lac@MnSNP, which had also been functionalised and stored under the same conditions (Fig. S3). This observation suggests the presence of Ostwald ripening, which occurred predominantly in smaller particles that probably did not contain MnO_2. Despite the structural rearrangement, both MnSNP and Lac@MnSNP retained their overall morphology and remained effective in detecting L-lactate, respectively. The stability of Lac@MnSNP upon to lactate was further confirmed by DLS analysis. Both MnSNP and Lac@MnSNP exhibited changes in hydrodynamic size upon interaction with the analyte (Table S2). Nevertheless, both nanoparticle types remained stable in the presence of the analyte, maintaining their morphology, as confirmed by TEM (Fig. 3).

In addition to the elemental analysis, X-ray photoelectron spectroscopy (XPS) was performed to further investigate the chemical composition of the probe and any changes induced by H_2O_2 treatment. Measurements taken at different positions across the samples indicated a homogenous elemental distribution. Furthermore, in repeated measurements, at the sample position, under the same experimental conditions, neither the

X-ray radiation nor the electrons/ions from the charge neutraliser system had any detectable effect on the recorded spectra.

High-resolution XPS elemental scans were performed on MnO_2, MnSNPs (treated and untreated with H_2O_2), and SNPs (Fig. 4). Trace amounts of potassium (~ 5 at%) were detected (Fig. 4(A)), likely originating from either residual KOH formed as a by-product of $KMnO_4$ reduction or incomplete reduction of $KMnO_4$ (see eqn (1)). The MnO_2 sample exhibited characteristic peaks for oxygen (Fig. 4(B)) and manganese (Fig. 4(C)), along with minor carbon contamination.

XPS analysis also confirmed that the chemical composition and structure of SNPs remained unchanged following H_2O_2 treatment (Table S1 and Fig. 4(B) and (D)). The silicon-to-oxygen (Si : O) atomic ratio in MnSNP was 23 : 59 before treatment and 26 : 60 after treatment, with no significant changes in the spectral position or shape of the O 1s and Si 2p peaks. A minor nitrogen signal (<1 at%) was detected, confirming successful functionalisation of the SNP surface with amino groups from APTMS (Fig. 1(B)-iii). The elemental concentrations derived from the XPS survey scans (Fig. 4(F)) are summarised in Table S1. Reference spectra for various manganese compounds have been extensively studied in the literature.[31,32] In this work, the binding energy maximum of the Mn $2p_{3/2}$ peak for MnO_2 was observed at 642.5 eV (Fig. 4(C)), which is consistent with reported values – for example, Ilton et al. reported the Mn$2p_{3/2}$ peak for MnO_2 at approximately 642 eV.[32] Additionally, the peak exhibited a tail extending towards lower binding energies (Fig. 4(E)), which can be attributed to the presence of Mn^{3+}.[31] No signals corresponding to metallic Mn or Mn^{2+} were detected, as these would appear at binding energies ≤ 641 eV.

Fitting of the Mn $2p_{3/2}$ peak, using literature-based multiplet splitting components for Mn^{4+} and Mn^{3+},[32] revealed a mixture

Table 2 EDX analysis of the particles before and after H_2O_2 treatment. The values are reported as weight percentage (w%). The extra elements found in the analysis include Na, K and Au

H_2O_2 treat.	MnO_2		MnSNP	
	Before	After	Before	After
Mn	33 ± 2	—	7 ± 2	—
Si	—	—	28 ± 2	25 ± 2
O	51 ± 4	—	54 ± 4	57 ± 1
C	13 ± 0	—	9 ± 0	16 ± 1
Extra	3 ± 1	—	2 ± 1	2 ± 0

This journal is © The Royal Society of Chemistry 2025

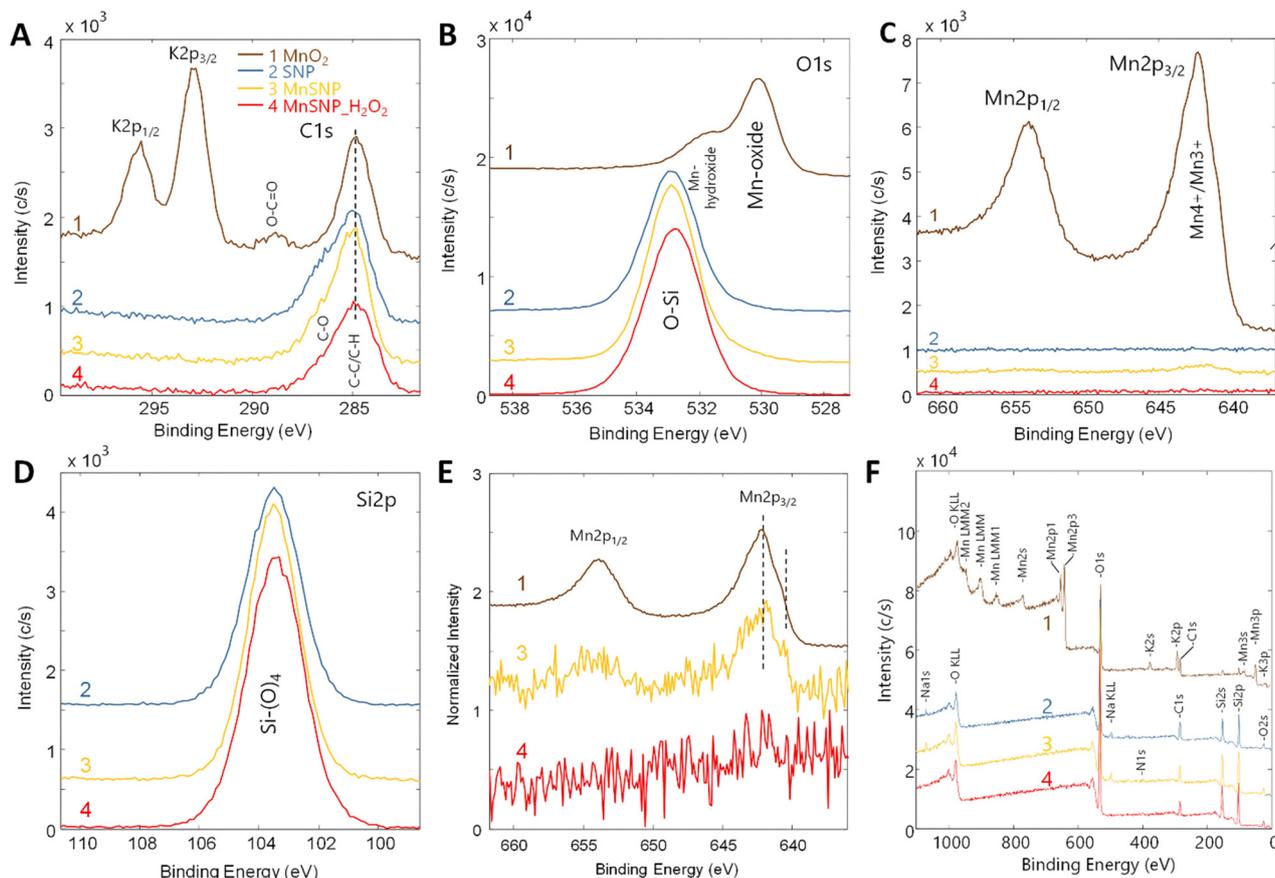J. Mater. Chem. B, 2025, 13, 11640–11651 | 11643

Fig. 4 Comparison of XPS high-resolution spectra for MnO_2 (brown line, 1), SNP (blue line, 2), MnSNP (yellow line, 3) and H_2O_2 treated MnSNP (red line, 4) for the elements (A) carbon C 1s and K 2p, (B) oxygen O 1s, (C) manganese Mn 2p, (D) silicon Si 2p. The thin vertical line in (A) marks the C–C bond, which was referenced to 284.8 eV. (E) Normalised signal intensity of one related to Mn 2p. The spectra are offset in the y-direction for better visualisation. (F) Comparison of XPS survey scans for MnO_2, SNP, MnSNP as well as H_2O_2 treated MnSNP. For better visualisation, scans 1 to 3 are offset in the y-direction compared to scan 4.

of Mn^{4+} (43%) and Mn^{3+} (57%) in the synthesised MnO_2. In comparison, the commercially available MnO_2 used as a reference contained only ∼30% Mn^{3+}, in agreement with previous reports.[32] The higher Mn^{3+} content in our synthesised material is attributed to the in-house production of MnO_2 via the $KMnO_4$ reduction method. Consistent with EDX results, XPS confirmed the presence of surface MnO_2 following its incorporation into the SNPs. Fig. 4(E) shows a weak Mn signal (0.4 at%, Table S1) in MnSNPs. Moreover, the shape and the binding energy of the Mn 2p spectrum remained unchanged between the MnO_2 and MnSNP samples (Fig. 4(E)), indicating that the chemical structure of MnO_2 was preserved during incorporation. After treatment with H_2O_2, the Mn signal disappeared from the XPS spectra (Fig. 4(C) and (E)), consistent with the transformation of MnO_2 into soluble Mn^{2+} and its subsequent dissolution, corroborating the EDX findings.

A stability test was conducted to compare the behaviour of MnSNPs (1 mg mL^{-1}) and MnO_2 in deionised water after 7 days of storage. MnO_2 was tested at two different concentrations: 0.01 mg mL^{-1}, which visually matched the colour of MnSNPs at 1 mg mL^{-1}, and 0.025 mg mL^{-1}, which exhibited similar absorbance values to MnSNPs at the same concentration. After

7 days, MnSNPs showed no change in the absorbance of the supernatant, whereas MnO_2 samples exhibited a decrease in absorbance to 0.98 and 0.88 at 0.01 mg mL^{-1} and 0.025 mg mL^{-1}, respectively, being the days of 0.025 mg mL^{-1} MnO_2 statistically different (p-value < 0.05) (Fig. S3A). Additionally, MnO_2 displayed a higher degree of agglomeration compared to MnSNPs during storage (Fig. S3B). Evidence of matrix rearrangement in MnSNPs was also observed on day 7 (Fig. S3C), likely due to Ostwald ripening – a common phenomenon in silica-based systems. Overall, the stability test confirmed that embedding MnO_2 within the silica matrix not only prevents the spontaneous dissolution observed in free MnO_2 but also significantly reduces particle agglomeration (Fig. S3B).

The selection of SNPs was guided by two main factors: (i) the ease with which their surface can be functionalised, enabling straightforward conjugation of the enzyme lactate oxidase; and (ii) the optical properties of silica. The optimal concentration of MnSNPs was determined by varying both amount of MnO_2 loaded within the SNPs (Fig. S4A) and the concentration of MnSNPs used in the assay (Fig. S4B), in order to achieve suitable absorbance for detecting the desired range of L-lactate. This study confirmed that higher availability of

11644 | J. Mater. Chem. B, 2025, 13, 11640–11651

This journal is © The Royal Society of Chemistry 2025

MnO_2 – whether through increased MnO_2 loading or higher MnSNP concentration – resulted in greater H_2O_2 detection, but with reduced sensitivity. Specifically, we observed that using high concentrations of MnO_2 particles diminished detection sensitivity due to a shielding effect, whereby small signal variations become undetectable. Based on NMR results, bacteria-producing lactate in urine samples is expected to range from 59 to 241 μg mL^{-1}, corresponding to bacterial concentrations of 10^3 to 10^5 CFU mL^{-1}, respectively.[33] Therefore, we set a working concentration of MnSNPs at 2 mg mL^{-1}, which corresponds to 26.9 μg mL^{-1} of MnO_2 particles, as determined spectrophotometrically using a calibration curve. This concentration was chosen to enhance the sensitivity of the method.

The detection efficacy of the probe was initially evaluated by treating 2 mg mL^{-1} MnSNPs with varying concentrations of H_2O_2 ranging from 0 to 100 μM. An incubation time of 4 hours was selected, as it yielded a more stable signal (Fig. S5). Results are reported as relative absorbance, calculated as the ratio of the absorbance intensity at each H_2O_2 concentration to that of the untreated sample $[I_n/I_0]$. The absorbance at 400 nm decreased linearly with increasing H_2O_2 concentration, reaching 0.78 relative absorbance at 50 μM of H_2O_2 ($R^2 = 0.94$), and further declining slightly to 0.67 at 100 μM (Fig. 5(B)). The limit of detection (LOD) was determined from the linear portion of the response curve, yielding an LOD of 26 μM for H_2O_2. To validate the detection mechanism, 2 mg mL^{-1} of Lac@MnSNP

was tested against L-lactate. A faster response was observed in the range of 50–100 μM L-lactate when the nanoparticles were functionalised with higher concentrations of lactate oxidase (Fig. S6). Two enzyme concentrations were evaluated: 50 μg mL^{-1} and 100 μg mL^{-1}. After 2 h of incubation, the probe containing 50 μg mL^{-1} of enzyme exhibited a stabilised signal of 0.9 at 25 μM L-lactate. In contrast, the probe with 100 μg mL^{-1} of enzyme showed a linear decrease in absorbance, reaching 0.71 at 50 μM L-lactate ($R^2 = 0.81$). Extending the incubation time to 4 h enhanced the responsiveness of the 50 μg mL^{-1} enzyme probe, which reached a plateau at 75 μM L-lactate with a signal decrease to 0.64. A similar trend was observed for the 100 μg mL^{-1} enzyme probe, which exhibited a linear decrease to 0.70 at 100 μM L-lactate ($R^2 = 0.94$). Overall, the absorbance signal of Lac@MnSNP decreased with increasing L-lactate concentration, particularly up to 50 μM (Fig. 5(C)). At 100 μg mL^{-1} of enzyme concentration, the signal dropped to 0.70, with a calculated LOD of 31 μM ($R^2 = 0.94$).

Lactate oxidase catalyses the conversion of L-lactate to pyruvate in a 1 : 1 ratio, producing one molecule of H_2O_2 per L-lactate molecule oxidised. Both MnSNP and Lac@MnSNP exhibited a similar response, with a linear decrease in absorbance up to 50 μM of H_2O_2 and L-lactate, respectively. The corresponding LOD values were 26 μM for H_2O_2 and 31 μM for L-lactate. These results confirm the successful catalysis of L-lactate by Lac@MnSNP and its subsequent quantification *via* indirect detection of the generated H_2O_2. These results
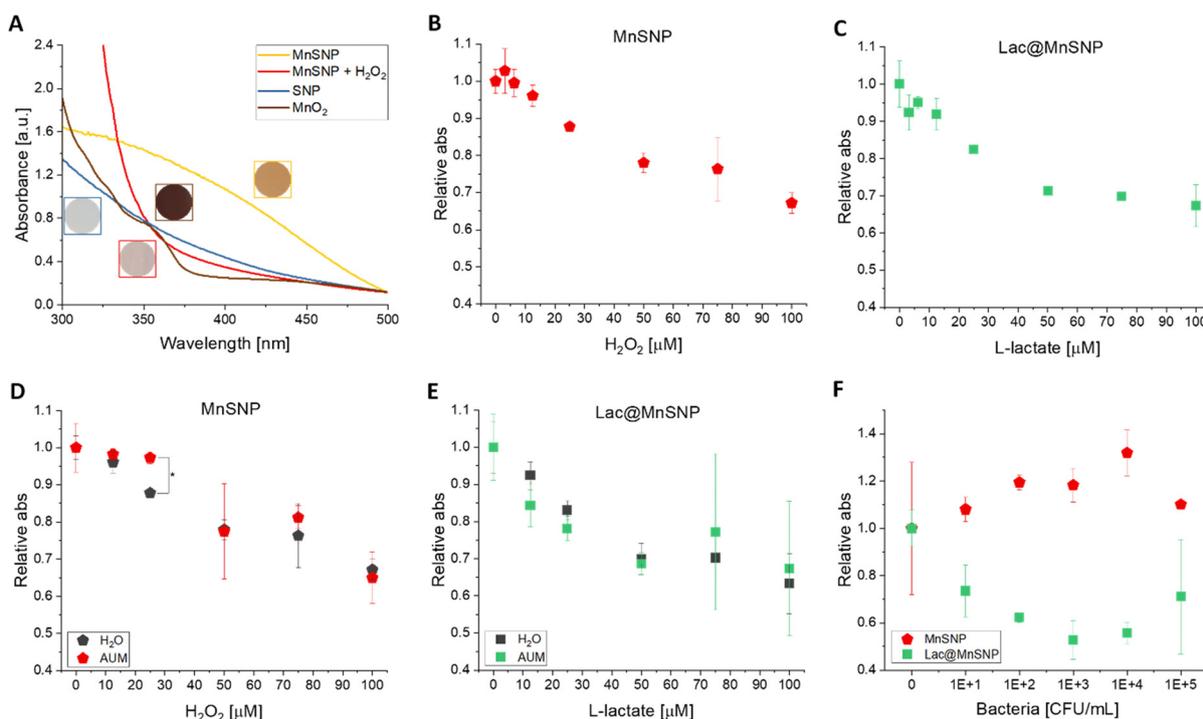
Fig. 5 Responsiveness of probe with H_2O_2 and L-lactate. (A) Absorbance values of MnO_2, SNP, and MnSNP before (MnSNP) and after interacting with H_2O_2 (MnSNP + H_2O_2). (B) Responsiveness of 2 mg mL^{-1} of MnSNP with H_2O_2 at 4 h. (C) Responsiveness of 2 mg mL^{-1} of Lac@MnSNP with L-lactate, after 4 h. Responsiveness of 2 mg mL^{-1} of (D) MnSNP with H_2O_2 and (E) Lac@MnSNP with L-lactate, in artificial urine medium (AUM), after 4 h. (F) Responsiveness of 2 mg mL^{-1} Lac@MnSNP with *E. faecalis* and *S. aureus*, after 5 h incubation. Data is reported as mean ± standard deviation (*n* = 3). Statistical analysis (ANOVA test and Tukey's test) were performed, to compare the different concentrations, and a two-sample *t*-test was performed to compare the concentrations of the different particles (*: $p < 0.05$).

This journal is © The Royal Society of Chemistry 2025

J. Mater. Chem. B, 2025, **13**, 11640–11651 | **11645**

confirm the detection mechanism of the designed probe, in which the presence of L-lactate leads to a decrease in absorbance, indirectly indicating the presence of *E. faecalis*. MnSNP was tested in PBS at different pH (*i.e.* pH 5, 6, 7 and 8) to mimic the different conditions of urine. The result showed that pH does not interfere with the detection efficacy of the probe further confirming the suitability for the proposed application (Fig. S7).

Given that urine is a complex matrix containing various components that could interfere with the probe's performance, MnSNP and Lac@MnSNP were tested in an artificial urine medium (AUM) to assess potential matrix effects. The absorbance spectra of AUM was analysed to see if it could interfere with the probe (Fig. S8). AUM did not present an absorbance peak at 400 nm wavelength, indicating that the probe is suitable for measurements in AUM and urine samples (Fig. S8). MnSNP and Lac@MnSNP were evaluated in DI water and AUM, using H_2O_2 and L-lactate as analytes, respectively (Fig. 5(D) and (E)). MnSNP exhibited similar responsiveness in both media, with a linear decrease in absorbance to 0.78 at 50 μM H_2O_2 and a further slight decrease to 0.67 at 100 μM. However, the sensitivity of the probe was reduced in AUM, with a LOD of 58 μM ($R^2 = 0.70$), compared to 26 μM in DI water.

Similarly, Lac@MnSNP showed comparable behaviour in both media, reaching a saturation point of 0.68 at 50 μM L-lactate in AUM, with an LOD of 47 μM ($R^2 = 0.86$), compared to 31 μM in DI water. These findings indicate that the complex composition of AUM affects the sensitivity of the probe. Nevertheless, the probe remains suitable for the intended application, as bacteria are known to produce 59–241 μg mL^{-1} of L-lactate during UTIs,[33] while normal urine does not typically contain L-lactate.[34,35]

As a proof-of-concept, the responsiveness of the probe was evaluated using the lactate-producing bacteria *E. faecalis* (Fig. 5(F)). The absorbance signal of 2 mg mL^{-1} Lac@MnSNP decreased linearly with increasing concentration of *E. faecalis*, reaching saturation at 10^3 CFU mL^{-1}. Further increases to 10^4 and 10^5 CFU mL^{-1} resulted in higher absorbance signals, likely due to exceeding the probe's detection range. It is important to note that UTIs are typically diagnosed when bacterial concentrations of $\geq 10^5$ CFU mL^{-1} for adults and 10^3–10^4 CFU mL^{-1} in children.[43,44] Depending on the diagnostic requirements, using higher concentrations of the probe could enable detection of bacterial loads above 10^3 CFU mL^{-1}. In contrast to Lac@MnSNP, MnSNP did not exhibit a decrease in signal upon

exposure to *E. faecalis* (Fig. 5(F)), confirming that the probe responds to lactate produced by the bacteria, and it is not affected by bacteria-related molecules, as no signal variation was measured using the enzyme-free probe (MnSNP). These results demonstrate the potential of the probe to discriminate between bacterial species through the detection of lactate produced by bacteria at concentrations up to 10^3 CFU mL^{-1} (*p*-value < 0.05), thereby contributing to improved diagnostics. Fig. 5(F) confirms that the probe responds to lactate produced by the bacteria, as no signal variation was measured when using the enzyme-free probe (MnSNP) in the presence of *E. faecalis.* The relation between the bacterial concentration and L-lactate detected was calculated using a calibration curve of the probe, when tested in water (Fig. S9). Concentrations of L-lactate of 56 μM were calculated for bacterial concentrations up to 10^3 CFU mL^{-1}. The calculated concentrations of L-lactate are above the LOD of the probe (31 μM), showing the potential of the probe in detecting bacterial load until 10^3 CFU mL^{-1}. The probe was also tested against the non-lactate-producing bacteria *Staphylococcus aureus* (*S. aureus*) (Fig. S10). In contrast to *E. faecalis*, Lac@MnSNP did not exhibit a decrease in signal upon exposure to *S. aureus*. These results demonstrate the potential of the probe to discriminate between bacterial species through the detection of lactate produced by bacteria. The proposed probe was compared with various L-lactate probes from the literature (Table 3) based on sensor type, incubation time, LOD, sample type, and application. As it is possible to observe, L-lactate-based sensors can be from different types of sensors, electrochemical,[36–38] fluorescent,[39–41] and colorimetric,[42] as is the case of this work presented, being colorimetric the least common type. Lac@MnSNP is composed of SNP and MnO_2 which are considered non expensive materials and is produced by a simple reverse microemulsion method. The majority of the sensors found in the literature use expensive materials such as multi-walled carbon nanotubes or metal–organic frameworks[38,39,41] or use complex synthesis methods,[36,41,42] turning the fabrication process more complex and less cost-effective. When comparing electrochemical and optical sensors, each type has its own advantages and disadvantages, electrochemical sensors may present a lower LOD, however, they also present more costly and complex fabrication processes.[36,38,45] When comparing fluorescent and colorimetric sensor probes, both solutions can be quantitative and qualitative, however, fluorescent sensors need the use of an external light source such as an UV lamp. Regarding the

Table 3 Comparison of Lac@MnSNP with L-lactate probes in the literature

Type of sensor	Incubation time	LOD$_{L\text{-lactate}}$	Type of sample	Application	Ref.
Electrochemical	1200 s	1.12×10^{-1} fM	Urine and blood	Diabetes	36
Electrochemical	5 h	66 μM	Tissue	Infection in wounds post-surgery	37
Electrochemical	5 s	55 pM	Sweat	Tissue oxygenation	38
Fluorescence	5 min	0.52 mM	Sweat	Health monitoring	39
Fluorescence	20 min	30 μM	Serum	POC chiral analysis in complexed biological samples	40
Fluorescence	N/A	0.091 μM	Milk and Sweat	Sports medicine, clinical environments, food industry	41
Colorimetric	N/A	0.63 mM	Urine	Liver disease	42
Colorimetric	4 h	31 μM	Urine	UTI	This work

health applications, L-lactate is used as a biomarker for monitoring the oxygenation levels of tissue,[38] infections[37] and other diseases such as diabetes or liver diseases,[36,42] being sweat the most common sample used.[38,39,41] In addition to this work, a colorimetric sensor that uses urine as a sample to determine the presence of a liver disease was found, presenting a LOD of 0.63 mM, roughly 20 times higher than the LOD of this work (31 μM).[42] The literature includes an L-lactate based sensor for the detection of infection in wounds post-surgery. The authors propose a wireless implantable electrochemical sensor for the identification of infection in orthopeadics, presenting an incubation time of 5 h and a LOD of 66 μM,[37] contrary to Lac@MnSNP, which presented a similar incubation time but a LOD of 31 μM. When comparing with the different sensors found in the literature, Lac@MnSNP presents a more cost-effective solution that has a LOD in the working range of the application. Regarding the sensors that use urine as a sample and sensors for infection-based application, Lac@MnSNP is one of the few examples of lactate-sensitive probe for the diagnosis of UTI in urine samples,[37,42] which is user friendly, cost-effective and presents a qualitative and quantitative solution with a low LOD and simple readout.

Conclusions

In this work, we present a colorimetric probe for the detection of *E. faecalis* in urine samples, based on detection of its metabolic by-product, L-lactate. Such strategy improves the reliability of the detection when compared with general pH-based approaches. Moreover, the proposed method is cost-efficient considering the simple preparation of the probe and the instrumentation required for the measurement. The probe, Lac@MnSNP, was validated against L-lactate, confirming the detection mechanism through indirect detection of H_2O_2. The sensitivity of the probe was evaluated, revealing an LOD of 31 μM for L-lactate. The probe remained stable following interaction with the analyte. The probe was also tested in AUM to mimic the complex environment of urine, where it was shown that Lac@MnSNP is not remarkably influenced by the components of urine, presenting a higher LOD of 47 μM, when comparing with DI water (LOD = 31 μM). Additionally, as a proof-of-concept, Lac@MnSNP was tested in the presence of *E. faecalis* and *S. aureus*. Lac@MnSNP successfully detected *E. faecalis*, a lactate-producing bacterium, up to 10^3 CFU mL^{-1}, showing its potential of detecting bacteria within the infection range. In contrast, Lac@MnSNP did not show a decrease in the signal when exposed to *S. aureus*, indicating that Lac@MnSNP is specific for L-lactate, and by extension, to bacteria that produces L-lactate as their metabolite. The probe demonstrated the potential as a novel POC diagnostic tool that enables a more accurate diagnosis of UTIs. By detecting bacteria-related analyte rather than physical and chemical parameters, as the current methods do, this colour-based sensor could enable more accurate diagnosis, and thus, more effective treatment of UTIs.

Experimental section

Materials

2-[4-(2,4,4-Trimethylpentan-2-yl)phenoxy]ethanol (Triton® X-100), 1-hexanol (anhydrous, ≥99%), cyclohexane (anhydrous, 99.5%), tetraethyl orthosilicate, (TEOS, ≥99%), ammonium hydroxide (28–30% in water), 3-(trihydroxysilyl)propyl methyl-phosphonate (THPMP, 50% in wt.% in H_2O), (3-aminopropyl)-trimethoxysilane (APTMS, 97%), manganese(IV) oxide (≥99%), potassium permanganate (≥99%), hydrogen peroxide (3% in wt% in H_2O), ethanol (≥99.8%), succinic anhydride (≥99%), and lactate oxidase from *Aeroccocus viridans* (lyophilised powder) were all purchased from Sigma Aldrich. Silica nanoparticles were synthesised as described below.

Instrumentation

Dynamic light scattering (DLS). The hydrodynamic sizes, zeta potential (ζ-potential), and polydispersity index (PDI) of the fabricated nanoparticles (NPs) were measured using a Zetasizer NanoZS (Malvern Instruments Ltd, Malvern, UK), equipped with a 633 nm HeNe laser and a backscatter detection angle of 90°. Samples were diluted to a final concentration of 50 μg mL^{-1} in deionised water (DI water). Measurements of size and PDI were performed using 1.5 mL disposable plastic cuvettes, while ζ-potential was measured using a disposable folded capillary cell (DTS1070, Malvern Instruments Ltd, Malvern, UK). All measurements were conducted at room temperature (~25 °C), and the reported values represent the average of three independent measurements.

UV-vis spectrophotometer. UV-Vis absorbance spectra were recorded using a Varian 50Bio spectrometer connected to a 50 Multi-Port Router (MPR) module (Agilent, Santa Clara, CA, USA). Samples were diluted to a concentration of 1 mg mL^{-1}, and 2 mL were transferred into a quartz cuvette. Spectra were collected over a wavelength range of 200–600 nm.

Microplate reader. The responsiveness of the probe to H_2O_2, L-lactate, and bacterial samples was monitored using a BioTek Synergy H1 microplate reader. Samples and media were added to a 96-well plate, with a final volume of 100 μL per well. UV-Vis absorbance spectra were recorded over a wavelength range of 230–999 nm.

NanoDrop spectrophotometer. Sample absorbance was measured using a NanoDrop One C spectrophotometer (Thermo-Fisher Scientific, Madison, WI, USA). A 1 μL aliquot of the sample was loaded onto the measurement pedestal and analysed using the "Protein E and M_W" setting (E = 51.340 M, M_W = 80 kDa).

Transmission electron microscopy (TEM). Samples were deposited onto carbon-coated copper grids (200 Mesh; Carbon Film Supported Copper Grid, Electron Microscopy Sciences, USA) and allowed to dry prior to imaging in REM Hitachi.

Energy-dispersive X-ray analysis (EDX). EDX analysis was performed using a Hitachi S-4800 scanning electron microscope operated at an accelerating voltage of 20 kV. Samples were mounted on conductive carbon tape, air-dried, and

This journal is © The Royal Society of Chemistry 2025

J. Mater. Chem. B, 2025, **13**, 11640–11651 | **11647**

subsequently sputter-coated with a thin layer of Au/Pd prior to imaging, using appropriate holders.

X-ray photoelectron spectroscopy (XPS). The surface chemical composition of the functionalised nanoparticles was analysed using a scanning XPS microprobe spectrometer (PHI VersaProbe II, Physical Electronics) equipped with monochromatic Al Kα radiation (1486.6 eV). A photoemission take-off angle of $45°$ relative to the sample surface was used. The analysis chamber was maintained at an operating pressure below 1.5×10^{-6} Pa, achieved *via* an ion pump.

Powder samples were pressed onto indium foil to create a flat, contiguous surface and mounted onto a stainless steel holder using double-sided adhesive tape. Minimal signal was detected from the indium substrate (<0.1 at%). Survey scans (0–1100 eV) were acquired with a step size of 0.8 eV, an acquisition time of 160 ms per data point, and an analyser pass energy of 187.85 eV.

High-resolution elemental spectra were collected for C 1s and K 2p (278–298 eV), O 1s (523–543 eV), Si 2p (94–114 eV), and Mn 2p (630–665 eV), using a step size of 0.125 eV, analyser pass energy of 29.35 eV, and acquisition times of 1.92 s (C, O, Si) and 4.8 s (Mn) time per data point. The energy resolution (FWHM, full width at half maximum height) was 2.2 eV for survey scans and 0.7 eV for high-resolution scans, as determined from the Ag $3d_{5/2}$ photoemission line. Total acquisition times were approximately 4 min for survey scans and 40 min for the five combined high-resolution scans.

Randomly selected spots on the samples were analysed using a micro-focused X-ray beam (100 μm diameter, 25 W at 15 kV). The $180°$ spherical capacitor energy analyser was operated in the fixed analyser transmission (FAT) mode. To compensate for potential sample charging, dual beam charge neutralisation was employed using a flux of low-energy electrons (1.3 eV) combined with very low-energy Ar^+ ions (10 eV).

The binding energy of the C 1s peak was referenced to 284.8 eV, corresponding to aliphatic carbon (C–C) from adventitious carbon contamination.[31] Atomic concentrations were calculated using CasaXPS software (version 2.3.16, Casa Software Ltd, Teignmouth, UK). Spectral fitting was performed using a mixed Gaussian–Lorentzian product function (70% Gaussian, 30% Lorentzian) to curve fit the XPS spectra (least-squares fitting routine) for determining the chemical bonding states of the various elements. A Shirley-type background was subtracted from the XPS peak areas.

Quantification was carried out using tabulated PHI sensitivity factors,[46] corrected for the instrument's transmission function and analyser asymmetry (accounting for the different angle between the X-ray source and analyser). Further detail on the XPS system and methodology have been previously published.[47]

Synthetic procedures

MnO$_2$-NP nanoparticles (MnNP). A 0.8 mL solution of KMnO$_4$ (125 mM) was added to a plastic reaction vessel. Subsequently, 200 μL of ammonia hydroxide (28–30%) was added to the solution. The reaction mixture was stirred continuously for 24 hours, at room temperature. The resulting product was collected by centrifugation at $6797 \times g$ for

8 minutes. The supernatant was discarded, and the pellet was resuspended in 1 mL of DI water using a probe sonicator (10% amplitude, 10 seconds). The resulting MnO$_2$ nanoparticle suspension was stored at 4 °C until further use.

MnO$_2$ loaded in silica nanoparticles (MnSNP). To prepare MnSNPs, 1.89 g Triton® X-100, 7.5 mL of cyclohexane, and 1.13 mL of 1-hexanol were added to a plastic vial. Then, 0.48 mL of the MnO$_2$ suspensions was introduced to form a microemulsion system, immediately followed by the addition of 100 μL of TEOS. After 30 minutes of stirring, 40 μL of ammonia hydroxide was added, and the reaction mixture was stirred for 24 hours.

Subsequently, 50 μL of TEOS was added, followed by 40 μL of THPMP after 20 minutes, and 10 μL of APTES after 5 minutes. The mixture was left for 24 hours.

Purification was carried out *via* three cycles of centrifugation at $15\,294 \times g$ for 8 minutes, followed by redispersion of the pellet using a probe sonicator (10% amplitude, 3 seconds). The final MnSNPs were suspended in deionised water (DI water) and stored at 4 °C.

As a control, pristine SNPs were synthesised using the same procedure, substituting the MnO$_2$ suspension with 0.48 mL of DI water during the microemulsion formulation step.

MnSNP functionalised with lactate oxidase (Lac@MnSNP). A suspension of MnSNPs (2 mg mL^{-1}) were reacted with succinic anhydride (1 mM) at room temperature for 1 hour under shaking ($41 \times g$). The particles were then isolated by centrifugation ($6797 \times g$, 8 minutes) and gently dispersed in Milli-Q water using a probe sonicator (10% amplitude, 3 seconds).

The resulting functionalised particles were incubated with varying concentrations of lactate oxidase (50 and 100 μg mL^{-1}) for 12 hours at room temperature under shaking at $41 \times g$. After incubation, the particles were collected by centrifugation ($6797 \times g$, 8 minutes) and gently redispersed in Milli-Q water using a vortex mixer. The resulting Lac@MnSNPs were either used immediately for assay or stored at 4 °C for a maximum of 24 hours.

Artificial urine medium. Artificial urine medium (AUM) was prepared by adapting protocols reported in the literature.[48] The following components were mixed in 100 mL of DI water: urea (310 mM), Na$_2$SO$_4$ (29.6 mM), KH$_2$PO$_4$ (19.8 mM), creatinine (1 mM), MgCl$_2$ (3.2 mM), NaCl (2.67 mM), CaCl$_2$ (2.6 mM), and KCl (1.55 mM). The prepared AUM solution was stored at 4 °C until further use.

Experiments

Stability test. Two sets of Eppendorf tubes were prepared, each containing 1 mL of either MnO$_2$ or MnSNP suspensions, for evaluation on day 1 and day 7. MnSNP suspension was prepared at a concentration of 1 mg mL^{-1}. MnO$_2$ suspension was prepared at two concentrations: 0.025 mg mL^{-1} (to match the absorbance of MnSNP) and 0.01 mg mL^{-1} (to match the visual colour of MnSNP).

On the respective day of analysis, the samples were centrifuged at $6797 \times g$ for 8 minutes. The absorbance at 400 nm was measured for both the supernatant and resuspended pellet to

11648 | *J. Mater. Chem. B*, 2025, **13**, 11640–11651

This journal is © The Royal Society of Chemistry 2025

evaluate the stability and retention of optical properties over time.

H₂O₂ assay. Stock solutions of MnSNP (2, 3, 4, and 5 mg mL⁻¹ in DI water) and H_2O_2 (31.2, 62.5, 125, 250, 500, 1000, and 2000 μM) were previously prepared. In a 96-well plate, 50 μL of MnSNP solution was mixed with 50 μL of H_2O_2 solutions, resulting in final MnSNP concentrations of 1, 1.5, 2, and 2.5 mg mL⁻¹, and final H_2O_2 concentrations of 15.6, 31.2, 62.5, 125, 250, 500, and 1000 μM. Control wells were prepared by MnSNP solutions with 50 μL of DI water.

Absorbance spectra were recorded after 2 h and 4 h of incubation using a microplate reader. Prior to measurement, samples were gently mixed using a pipette. Absorbance was measured at 400 nm.

L-lactate assay. Lac@MnSNPs were isolated by centrifugation at 6797 × g for 8 min and redispersed in 500 μL of Milli-Q water, yielding 3 stock solutions at a concentration of 4 mg mL⁻¹. Stock solutions of L-lactate (6.25, 12.5, 25, 50, 100, 150, and 200 μM) were previously prepared in DI water.

In a 96-well plate, 50 μL of Lac@MnSNP and 50 μL L-lactate were added in each well, resulting in final concentrations of 2 mg mL⁻¹ for Lac@MnSNP and 3.13, 6.25, 12.5, 25, 50, 75, and 100 μM for L-lactate. Control wells were prepared by mixing Lac@MnSNP with 50 μL of Mili-Q water.

Absorbance spectra were recorded after 2 and 4 h of incubation using a microplate reader. Prior to measurement, samples were gently mixed using a pipette. Absorbance was measured at 400 nm.

Bacterial assay. *Enterococcus faecalis* (DSM 20478) and *Staphylococcus aureus* (DSM 2569) were cultured overnight on TSY-Agar plates. The following day, bacterial colonies were collected and inoculated in 30% TSB incubated overnight at 37 °C. A working bacterial suspension was then prepared in 4-(2-hydroxyethyl)piperazine-1-ethanesulfonic acid (HEPES) buffer (10 mM) supplemented with glucose (2.5 mM), adjusted to an optical density of 0.1 at 600 nm (OD_{600}). Serial dilutions were performed to obtain final concentrations of 10^5, 10^4, 10^3, 10^2, and 10^1 CFU mL⁻¹.

MnSNP and Lac@MnSNP stock solutions (4 mg mL⁻¹) were prepared in the same HEPES + glucose medium. In a 96-well plate, 50 μL of nanoparticle solution and 50 μL of diluted bacterial suspension were combined, resulting in a final nanoparticle concentration of 2 mg mL⁻¹. Control wells include bacteria alone and nanoparticles alone in HEPES + glucose. Bacteria growth and MnO_2 reduction were monitored by measuring absorbance at 600 nm and 400 nm, respectively, using a microplate reader.[49] Measurements were taken hourly over an 8-hour period, with gentle mixing before each read to resuspend aggregates and ensure accurate readings.

Statistics. Statistical analysis was conducted using the Origin 2022 software. The different samples were compared through an ANOVA test with a *post-hoc* analysis ($\alpha = 0.05$), including Tukey's test, Levene's test, and actual power calculation. To compare the different particles, a *t*-test was performed (two-sample *t*-test, $\alpha = 0.05$, actual power).

The limit of detection (LOD) was determined from the linear region of the calibration curves using a linear region model.

LOD was calculated using the formula: 3.3σ/slope, where σ represents the standard deviation of the blank measurements.

Author contributions

MMM: investigation, data curation, conceptualization, writing, review-editing. AM: investigation, data curation. PR: investigation, data curation, review-editing. SA: investigation, data curation, review-editing. QR: investigation, review-editing. LFB: conceptualization, review-editing. GG: funding acquisition, conceptualization, project administration, data curation, writing, review-editing. All authors have approved the final version of the manuscript.

Conflicts of interest

There are no conflicts to declare.

Data availability

The data supporting this article have been included as part of the SI and can be available from the corresponding author upon reasonable request. See DOI: https://doi.org/10.1039/d5tb01437a

Acknowledgements

Notes and references

1 M. Medina and E. Castillo-Pino, An introduction to the epidemiology and burden of urinary tract infections, *Ther. Adv. Urol.*, 2019, **11**, 1756287219832172.

2 A. L. Flores-Mireles, J. N. Walker, M. Caparon and S. J. Hultgren, Urinary tract infections: epidemiology, mechanisms of infection and treatment options, *Nat. Rev. Microbiol.*, 2015, **13**(5), 269–284.

3 M. Li, F. Yang, Y. Lu and W. Huang, Identification of *Enterococcus faecalis* in a patient with urinary-tract infection based on metagenomic next-generation sequencing: a case report, *BMC Infect. Dis.*, 2020, **20**(1), 467.

4 H. Kettler, K. White and S. J. Hawkes, Research UNWBWSPf, Training, in *Tropical D. Mapping the landscape of diagnostics for sexually transmitted infections: key findings and recommendations*, ed. H. Kettler, K. White and S. Hawkes, World Health Organization, Geneva, 2004.

5 R. S. Matulewicz, J. O. DeLancey, E. Pavey, E. M. Schaeffer, O. Popescu and J. J. Meeks, Dipstick Urinalysis as a Test for Microhematuria and Occult Bladder Cancer, *Bladder Cancer*, 2017, **3**(1), 45–49.

This journal is © The Royal Society of Chemistry 2025

J. Mater. Chem. B, 2025, **13**, 11640–11651 | 11649

6 E. Lepowsky, F. Ghaderinezhad, S. Knowlton and S. Tasoglu, Based assays for urine analysis, *Biomicrofluidics*, 2017, **11**(5), 051501.

7 N. M. Maalouf, M. A. Cameron, O. W. Moe and K. Sakhaee, Novel insights into the pathogenesis of uric acid nephrolithiasis, *Curr. Opin. Nephrol. Hypertens.*, 2004, **13**(2), 181–189.

8 P. S. Guiton, T. J. Hannan, B. Ford, M. G. Caparon and S. J. Hultgren, *Enterococcus faecalis* overcomes foreign body-mediated inflammation to establish urinary tract infections, *Infect. Immun.*, 2013, **81**(1), 329–339.

9 C. A. Arias and B. E. Murray, The rise of the Enterococcus: beyond vancomycin resistance, *Nat. Rev. Microbiol.*, 2012, **10**(4), 266–278.

10 European Centre for Disease P, Control, World Health Organization. Regional Office for E. Antimicrobial resistance surveillance in Europe 2022 – 2020 data. Copenhagen: World Health Organization. Regional Office for Europe; 2022 2022.

11 World Health O. WHO bacterial priority pathogens list, 2024: bacterial pathogens of public health importance, to guide research, development and strategies to prevent and control antimicrobial resistance. Geneva: World Health Organization; 2024.

12 E. Fiore, D. V. Tyne and M. S. Gilmore, Pathogenicity of Enterococci, *Microbiol. Spectrum*, 2019, **7**(4), DOI: **10.1128/microbiolspec.gpp3-0053-2018**.

13 A. I. Hidron, J. R. Edwards, J. Patel, T. C. Horan, D. M. Sievert and D. A. Pollock, *et al.*, Antimicrobial-Resistant Pathogens Associated With Healthcare-Associated Infections: Annual Summary of Data Reported to the National Healthcare Safety Network at the Centers for Disease Control and Prevention, 2006–2007, *Infect. Control Hosp. Epidemiol.*, 2008, **29**(11), 996–1011.

14 A. L. Kau, S. M. Martin, W. Lyon, E. Hayes, M. G. Caparon and S. J. Hultgren, *Enterococcus faecalis* Tropism for the Kidneys in the Urinary Tract of C57BL/6J Mice, *Infect. Immun.*, 2005, **73**(4), 2461–2468.

15 C. S. Pundir, V. Narwal and B. Batra, Determination of lactic acid with special emphasis on biosensing methods: A review, *Biosens. Bioelectron.*, 2016, **86**, 777–790.

16 G. Yang, J. Hong and S.-B. Park, Wearable device for continuous sweat lactate monitoring in sports: a narrative review, *Front. Physiol.*, 2024, **15**, 1376801.

17 R. Beneke, R. M. Leithäuser and O. Ochentel, Blood lactate diagnostics in exercise testing and training, *Int. J. Sports Physiol. Perform.*, 2011, **6**(1), 8–24.

18 K. Berend and A. Duits, The role of the clinical laboratory in diagnosing acid–base disorders, *Crit. Rev. Clin. Lab. Sci.*, 2019, **56**(3), 147–169.

19 N. G. Kowlgi and L. Chhabra, d-lactic acidosis: an under-recognized complication of short bowel syndrome, *Gastroenterol. Res. Pract.*, 2015, **2015**(1), 476215.

20 G. Rattu, N. Khansili, V. K. Maurya and P. M. Krishna, Lactate detection sensors for food, clinical and biological applications: a review, *Environ. Chem. Lett.*, 2021, **19**(2), 1135–1152.

21 C. Liu, X. Sun, Q. Wang, S. Wang, Q. Wang and S. Zhang, State of the art Overview wearable microfluidic noninvasive biomarker sensors for sweat analysis, *Microchem. J.*, 2025, **209**, 112847.

22 S. R. S. Pour, D. Calabria, A. Emamiamin, E. Lazzarini, A. Pace and M. Guardigli, *et al.*, Electrochemical vs. Optical Biosensors for Point-of-Care Applications: A Critical Review, *Chemosensors*, 2023, **11**(10), 546.

23 S. Rasheed, T. Kanwal, N. Ahmad, B. Fatima, M. Najam-ul-Haq and D. Hussain, Advances and challenges in portable optical biosensors for onsite detection and point-of-care diagnostics, *TrAC, Trends Anal. Chem.*, 2024, **173**, 117640.

24 E. Vavrinsky, N. E. Esfahani, M. Hausner, A. Kuzma, V. Rezo and M. Donoval, *et al.*, The Current State of Optical Sensors in Medical Wearables, *Biosensors*, 2022, **12**(4), 217.

25 O. I. Guliy, O. A. Karavaeva, A. V. Smirnov, S. A. Eremin and V. D. Bunin, Optical Sensors for Bacterial Detection, *Sensors*, 2023, **23**(23), 9391.

26 C. Deusenbery, Y. Wang and A. Shukla, Recent innovations in bacterial infection detection and treatment, *ACS Infect. Dis.*, 2021, **7**(4), 695–720.

27 A. Malic, E. Ntrivalas and J. DuBois, Clinical performance and utility of point-of-care lactate technology in patient care pathways, *Point of Care*, 2019, **18**(2), 62–65.

28 I. S. Kucherenko, Y. V. Topolnikova and O. O. Soldatkin, Advances in the biosensors for lactate and pyruvate detection for medical applications: A review, *TrAC, Trends Anal. Chem.*, 2019, **110**, 160–172.

29 F. Pan, G. Giovannini, S. Zhang, S. Altenried, F. Zuber and Q. Chen, *et al.*, pH-responsive silica nanoparticles for the treatment of skin wound infections, *Acta Biomater.*, 2022, **145**, 172–184.

30 G. Giovannini, F. Kunc, C. C. Piras, O. Stranik, A. A. Edwards and A. J. Hall, *et al.*, Stabilizing silica nanoparticles in hydrogels: impact on storage and polydispersity, *RSC Adv.*, 2017, **7**(32), 19924–19933.

31 M. C. Biesinger, B. P. Payne, A. P. Grosvenor, L. W. Lau, A. R. Gerson and R. S. C. Smart, Resolving surface chemical states in XPS analysis of first row transition metals, oxides and hydroxides: Cr, Mn, Fe, Co and Ni, *Appl. Surf. Sci.*, 2011, **257**(7), 2717–2730.

32 E. S. Ilton, J. E. Post, P. J. Heaney, F. T. Ling and S. N. Kerisit, XPS determination of Mn oxidation states in Mn (hydr)oxides, *Appl. Surf. Sci.*, 2016, **366**, 475–485.

33 A. Gupta, M. Dwivedi, A. A. Mahdi, G. A. N. Gowda, C. L. Khetrapal and M. Bhandari, 1H-nuclear magnetic resonance spectroscopy for identifying and quantifying common uropathogens: A metabolic approach to the urinary tract infection, *BJU Int.*, 2009, **104**(2), 236–244.

34 N. Sarigul, F. Korkmaz and İ. Kurultak, A New Artificial Urine Protocol to Better Imitate Human Urine, *Sci. Rep.*, 2019, **9**(1), 20159.

35 C. Aubron, O. Huet, S. Ricome, D. Borderie, E. Pussard and P.-E. Leblanc, *et al.*, Changes in urine composition after trauma facilitate bacterial growth, *BMC Infect. Dis.*, 2012, **12**(1), 330.

11650 | *J. Mater. Chem. B*, 2025, **13**, 11640–11651

This journal is © The Royal Society of Chemistry 2025

36 R.-I. Stefan-van Staden, I. Popa-Tudor, C. Ionescu-Tirgoviste and R. A. Stoica, Molecular recognition of pyruvic acid and L-lactate in early-diabetic 1-type stage, *J. Electrochem. Soc.*, 2018, **165**(14), B659.

37 B. Gil, T. A. G. Hall, D. M. E. Freeman, D. Ming, S. Kechagias and S. Nabilla, *et al.*, Wireless implantable bioelectronics with a direct electron transfer lactate enzyme for detection of surgical site infection in orthopaedics, *Biosens. Bioelectron.*, 2024, **263**, 116571.

38 B. Tao, W. Yang, F. Miao, Y. Zang and P. K. Chu, A sensitive enzyme-free electrochemical sensor composed of Co_3O_4/CuO@MWCNTs nanocomposites for detection of L-lactic acid in sweat solutions, *Mater. Sci. Eng., B*, 2023, **288**, 116163.

39 Y. Jia and B. Yan, Visual ratiometric fluorescence sensing of L-lactate in sweat by Eu-MOF and the design of logic devices, *Spectrochim. Acta, Part A*, 2023, **297**, 122764.

40 J. Xu, M. Wang, M. Li, J. Yang and L. Yang, Based chiral biosensors using enzyme encapsulation in hydrogel network for point-of-care detection of lactate enantiomers, *Anal. Chim. Acta*, 2023, **1279**, 341834.

41 B. Jing, X. Xu, J. Wang, C. Sun, W. Li and Z. Chang, Highly sensitive and selective L-lactate monitoring in complex matrices with a ratiometric fluorescent sensor RhB@Zn-MOF, *J. Environ. Chem. Eng.*, 2024, **12**(6), 114233.

42 E. Evans, E. F. M. Gabriel, T. E. Benavidez, W. K. T. Coltro and C. D. Garcia, Modification of microfluidic paper-based devices with silica nanoparticles, *Analyst*, 2014, **139**(21), 5560–5567.

43 T. T. Kouri, W. Hofmann, R. Falbo, M. Oyaert, S. Schubert and J. B. Gertsen, *et al.*, The EFLM European urinalysis guideline 2023, *Clin. Chem. Lab. Med.*, 2024, **62**(9), 1653–1786.

44 A. D. Hay, K. Birnie, J. Busby, B. Delaney, H. Downing and J. Dudley, *et al.*, The Diagnosis of Urinary Tract infection in Young children (DUTY): a diagnostic prospective observational study to derive and validate a clinical algorithm for the diagnosis of urinary tract infection in children presenting to primary care with an acute illness, *Health Technol. Assess.*, 2016, **20**(51), 1–294.

45 O. Pashchenko, T. Shelby, T. Banerjee and S. Santra, A Comparison of Optical, Electrochemical, Magnetic, and Colorimetric Point-of-Care Biosensors for Infectious Disease Diagnosis, *ACS Infect. Dis.*, 2018, **4**(8), 1162–1178.

46 J. Moulder, W. Stickle, P. Sobol and K. Bomben, *Handbook of X-ray Photoelectron Spectroscopy*, Physical Electronics, Inc., Eden Prairie, MN, 1995.

47 P. Rupper, M. Amberg, D. Hegemann and M. Heuberger, Optimization of mica surface hydroxylation in water vapor plasma monitored by optical emission spectroscopy, *Appl. Surf. Sci.*, 2020, **509**, 145362.

48 P. Bhatt, D. Kukkar, A. K. Yadav and K. H. Kim, Carbon dot-copper nanocomposite-based fluorescent sensor for detection of creatinine in urine samples of CKD patients, *Spectrochim. Acta, Part A*, 2024, **307**, 123666.

49 F. Pan, S. Altenried, S. Scheibler, I. Rodriguez Fernandez, G. Giovannini and Q. Ren, Ultrafast determination of antimicrobial resistant staphylococcus aureus specifically captured by functionalized magnetic nanoclusters, *ACS Sens.*, 2022, **7**(11), 3491–3500.

This journal is © The Royal Society of Chemistry 2025

J. Mater. Chem. B, 2025, **13**, 11640–11651 | **11651**